EFFECT OF WATER-CEMENT RATIO AND CURRENT DENSITY ON ACCELERATED CORROSION-INDUCED CRACKING

ISMAIL ALDELLAA and PETER GRASSL*

University of Glasgow
Oakfield Avenue, Glasgow G12 8LT, United Kingdom
*e-mail: peter.grassl@glasgow.ac.uk

Key words: Corrosion rate; concrete cracking; creep; lattice modelling

Abstract. It is not fully understood how corrosion-induced cracking in reinforced concrete is affected by corrosion rate. Improved understanding of this effect is important because it assists with predicting the state of structures which suffer from corrosion-induced cracking based on results of accelerated laboratory tests with confidence. Possible reasons for the effect of corrosion rate on corrosion-induced cracking are creep of concrete, migration of corrosion products into pores and cracks, and composition of corrosion products. Here, we test the effect of creep. We carry out corrosion experiments on specimens consisting of a single reinforcement bar embedded in a concrete cylinder. We vary corrosion rates and water-cement ratios of concrete. The modelling of corrosion-induced cracking is carried out with a lattice approach based on a visco-elastic damage-plasticity constitutive model which predicts the effects of linear creep, but not the migration of corrosion products nor the effect of corrosion rate on corrosion products. With this choice of model, we test if creep together with fracture can reproduce the effects of water-cement ratio and corrosion rates. Based on our experimental results, corrosion penetration at a fixed surface crack width increases with decreasing corrosion rate and increases with increasing water-cement ratio. The lattice approach with fracture and creep but without corrosion product migration is not able to reproduce the dependencies of rate and water-cement ratio on critical corrosion penetration satisfactorily.

1 INTRODUCTION

Corrosion of steel in reinforced concrete is a commonly encountered deterioration process, which is divided into an initiation (before the onset of corrosion) and propagation stage (after the onset of corrosion) [37]. During the propagation stage investigated in this study, corrosion products build up close to the concrete-steel interface. These corrosion products are of greater volume than steel and, therefore, compress radially the surrounding concrete. Compression is equilibrated by tensile stresses, which typically result in cracking and spalling of concrete cover. Corrosion may lead to significant loss of steel area, which affects the ultimate limit state

of structures [12].

The process of naturally occurring corrosion in reinforced concrete is very slow. It often takes many decades before corrosion results in structural damage [20, 14]. Therefore, experiments on corrosion-induced cracking are usually accelerated. Laboratory tests in which the environment of the reinforced specimens are made more aggressive by means of exposure to salt fog are reported in François and Arliguie [20], Zhang et al. [41, 42, 43]. Results are obtained even quicker by speeding up the depassivation of the reinforcement by adding chlorides and accelerating the flow of electrons by impressed current [6, 30, 18]. A wide range of

impressed current densities from 3 μA/cm^2 in Alonso et al. [4] to 10400 μA/cm^2 in Almusallam et al. [3] have been used. For low currents, the onset of cracking can occur after a year [4], whereas for high currents it has been reported to occur after a few hours [3]. It is known that most naturally occurring current densities during steel corrosion in concrete are between 0.1 μA/cm^2 and 10 μA/cm^2, but can occasionally reach 100 μA/cm^2 [12], which is the most used current density for acceleration with impressed currents [6, 4, 5].

It is still not fully understood what the effect of current density on the link between corrosion penetration (transformation of steel into corrosion products) and the cracking process is. The majority of experimental studies on corrosion-induced crack initiation and propagation use small ranges of current densities and water-cement ratios [4, 38, 32, 40, 29]. Only in a few studies either water-cement ratio or current density is varied. Water-cement ratio was varied in Alonso et al. [4], Vu et al. [38], Mullard and Stewart [32] but the current density was kept constant. In these studies, it was shown that the greater the water-cement ratio is, the smaller is the crack opening at a constant corrosion penetration. In Zhang et al. [44], the effect of rate on the composition of corrosion products was studied.

Possible reasons for these trends are suitably explored by numerical modelling as done in this study. Structural analyses approaches based on 3D/2D spatial discretisation of the specimen using finite element method [9] and discrete approaches [35, 11, 23] are well suited for modelling crack evolution and have been used for corrosion-induced cracking [31, 19, 2, 28]. These spatial discretisation approaches are suitable for modelling asymmetric crack evolution, nonuniform corrosion and the effect of multiple reinforcement bars.

This study aims to investigate if creep has a strong effect on corrosion-induced cracking. For the numerical approach, we choose a visco-elastic damage-plasticity lattice model proposed in a recent numerical study reported

in Aldellaa et al. [2]. This approach has been shown to be suitable for modelling fracture using plasticity and damage and for predicting linear creep by the visco-elastic part of the model. The heterogeneity of concrete is modelled by spatially autocorrelated fields. By design, migration of rust and changes of composition of corrosion products is not taken into account in the numerical modelling approach, because we want to test if creep together with fracture can predict the experimentally observed effects of current density on the relation of crack width and corrosion penetration. For the experimental part of this study, we investigated both the effect of current density (50, 100, and 500 μA/cm^2) and water-cement ratio (0.38, 0.45, 0.55 and 0.7) on the relation of crack width and corrosion penetration.

2 EXPERIMENTAL PROCEDURE

Corrosion-induced cracking experiments accelerated by an impressed current are carried out. Both current density and water-cement ratio are varied. The test setup consists of a concrete cylinder with a single steel reinforcement bar in the centre as shown in Figure 1.
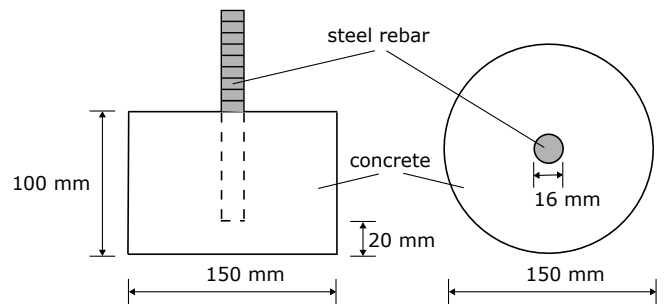

Figure 1: Geometry of test specimen.

The diameter and height of the concrete cylinder are 150 and 100 mm, respectively. The reinforcement bar has a diameter of 16 mm and is embedded in the concrete specimens up to a depth of 80 mm. The concrete cylinders were made by using four different concrete mixes called wc0p38, wc0p45, wc0p55 and wc0p70, with water-cement ratios 0.38, 0.45, 0.55 and 0.70, respectively. For all concrete mixes, Ordinary Portland Cement 32.5N was used. The

maximum aggregate size is 20 mm and 10 mm for two-thirds and one-third of the total content of aggregate, respectively. A concentration of 2 % of sodium chloride NaCl by weight of cement (w/w) has been added to the mixtures to initiate corrosion. For each mix, 9 cylinders were cast, so that there are three specimens of the same mix for each current density.

The specimens were placed in water at a constant temperature of 20 C° one day after mixing and were left in water until testing. Three cubes of each mix were tested in compression to determine compressive strength f_{c28} at the age of 28 days. Based on this compressive strength, tensile strength f_t, Young's modulus E and fracture energy G_F were calculated according to the *fib* Model Code 2010 formulae. The values for these properties at 28 days and the concrete age at which the corrosion tests were started are shown in Table 1.

Table 1: Concrete properties for four concrete mixes

	$f_{cm(28)}$ [MPa]	$f_{tm(28)}$ [MPa]	$E_{ci(28)}$ [GPa]	t_0 [days]
wc0p38	42.1	3.2	34.7	684
wc0p45	29.9	2.3	31.0	535
wc0p55	23.2	1.8	28.5	429
wc0p70	14.4	1.0	24.3	339

Corrosion was accelerated by means of impressed currents with current densities of 50, 100 and 500 $\mu A/cm^2$. A constant current was applied from a DC power supply to a control box with adjustable load channels to provide the three chosen current densities for this study. This adjusted current was then applied to the steel bar (anode) and copper mesh (cathode) by connecting the positive terminal with the bar and the negative terminal with the copper mesh. To ensure that the concrete specimen with the steel bar (anode) and the copper mesh (cathode) have electrical contact, both were immersed in sodium chloride solution with 5 per cent concentration. The experimental setup for three of the specimens is shown in Figure 2.
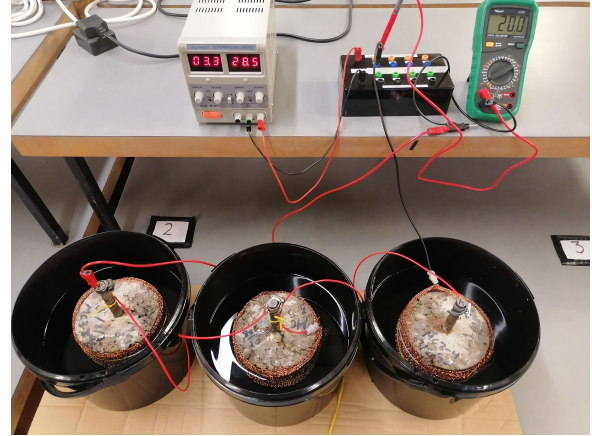
Figure 2: Experimental setup of the accelerated test.

During the testing, the value of the current passing through each test specimen was monitored continuously with a voltmeter to ensure that the current density remained constant at the desired value. To identify cracking on the concrete surface and to measure the crack width, a digital concrete crack width meter was used. The readings were taken several times a day during the early period of the test. At the end of the test, the mass of corrosion products was measured following standard practice according to ASTM Committee G01 Standard [36] and compared to theoretical predictions using Faraday's law [1], which provided a reasonable agreement.

3 LATTICE MODELLING

The experiments were simulated with a lattice model implemented in the finite element program OOFEM [33]. This section describes the lattice modelling approach for corrosion-induced cracking used in this study which was originally developed in Aldellaa et al. [2]. The present approach is a combination of two modelling concepts, where a lattice model based on a damage-plasticity constitutive model for fracture [21, 7] is combined with a linear creep model based on the Micro-Prestress Solidification (MPS) theory of concrete creep [25].

The lattice model belongs to the group of discrete techniques in which the fracture process is modelled as the failure of discrete

trusses, beams and rigid bodies [27, 16, 45, 34, 39, 17]. The present lattice approach is based on the rigid body spring concept first proposed in Kawai [27]. Extension of this rigid body concept for which the shape of rigid bodies is determined by Voronoi tessellation has been proven to be suitable for fracture simulations [39]. The constitutive models for these approaches are constructed in terms of tractions and displacement jumps similar to interface models for concrete fracture [13].

Within the lattice model, points are randomly placed in the domain to be analysed while enforcing a minimum distance between the points. A dual Voronoi and Delaunay tessellation based on this set of random points, provides the location of the nodes of discrete elements. The location of the lattice elements is determined from the edges of the Delaunay tessellation. The properties of the cross-section of the elements are obtained from the facets of the dual Voronoi tessellation [39] (Figure 3).
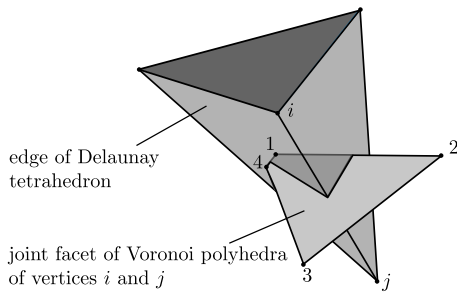
Figure 3: Geometrical relationship between Delaunay and Voronoi tessellations.

As shown in Figure 4, there are six Degrees Of Freedom (DOF) for the lattice element nodes, namely three displacements and three rotations.
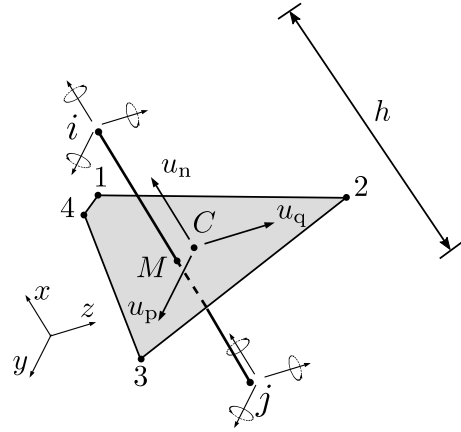
Figure 4: Lattice element with cross-section defined by the associated Voronoi facet.

From the DOFs, six displacement jumps at the centroid of the mid cross-section of the elements are computed. The three rotational jumps are related to effective moment like quantities via elastic relationships. The three translational jumps are used in a plasticity constitutive model to calculate the corresponding effective tractions [21]. All six components are reduced by damage.

The damage-plasticity constitutive model was adopted for concrete based on the work provided in [22, 21, 7]. The plasticity model uses a yield surface that is based on the normal component and the norm of the two shear components of the effective stress. The surface is composed of two ellipses as shown in Figure 5.
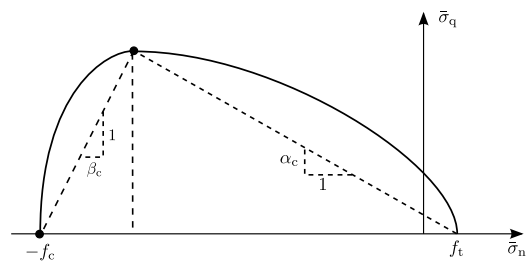
Figure 5: Yield surface.

Plastic flow is modelled with a plastic potential that differs from the yield function. This allows for the control of the amount of normal plastic strain. The damage variable is deter-

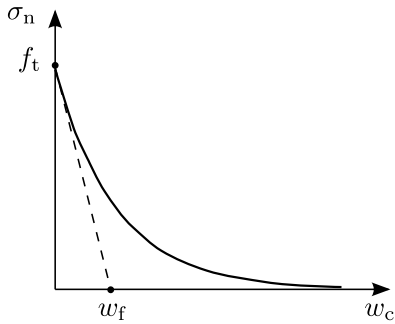mined from an exponential softening law shown in Figure 6.

Figure 6: Exponential softening law.

The damage-plasticity model requires a number of parameters. The macroscopic Young's modulus and Poisson's ratio are controlled by parameters E and a_1. Furthermore, to control the shape and the size of the yield surface the required parameters are $f_t, f_c, \alpha_c, \beta_c$ and A_h. Additionally, parameter ψ controls the plastic flow, and G_F controls the amount of dissipated energy during cracking. A detailed description of the equations containing these parameters is available in Grassl and Davies [21], Athanasiadis et al. [7].

The damage-plasticity model was extended to visco-elasticity for the special case of constant ambient temperature under hygrally sealed conditions. For this case, the response of the visco-elastic model is identical to the basic creep compliance function of the B3 model. The implementation of the MPS material model uses the rate-type approach summarised in "Algorithm 10.1: Incremental stress–strain relation according to the microprestress-solidification theory" [10]. Under sealed conditions this algorithm can be further simplified to "Algorithm 5.3: Exponential algorithm for solidifying Kelvin chain". Additionally, the parameters of the Dirichlet series are estimated from the continuous retardation spectrum [26] of the non-ageing compliance function, which makes the implementation more efficient.

The evolution of tensile and compressive strength with time in the visco-elastic exten-

sion of the damage-plasticity approach models was described by the *fib* Model Code 2010 formulae [15]. The damage-plasticity model is connected in series with the viscoelastic model. Accordingly, the total strain (stress-dependent) is divided into viscoelastic and inelastic components so that the stress transferred by the two models is equal. An iterative approach is used to satisfy this condition [2].

4 Analyses

The geometry and boundary conditions and calibration procedures used with the modelling approach are described in the following paragraphs. The geometry of the problem analysed is a concrete cylinder with a steel reinforcement bar at its centre. The inner radius which is the radius of the reinforcement bar is $r_i = 8$ mm and the outer radius of the concrete cylinder is $r_o = 75$ mm, with an out-of-plane thickness is 10 mm of the top layer of the cylinder as shown in Figure 7.
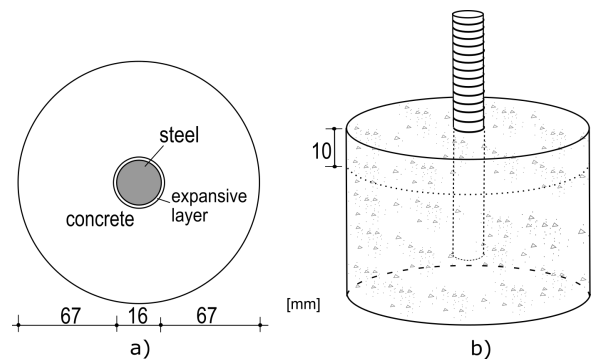

Figure 7: Concrete specimen: a) top view of a 10 mm slice of the concrete cylinder with the steel bar in the centre, b) 3D geometry of the cylinder with the steel bar.

The steel bar is discretised by lattice elements and the radial displacement induced by the formation of the corrosion products is modelled by inelastic displacements u_{cor} applied to elements adjacent to the concrete steel interface, which are set equal to corrosion penetration x_{cor} assuming an expansion factor of 2. Here, the corrosion penetration x_{cor} is calculated from Faraday's law as

$$x_{cor} = 0.032 i_{cor} t \tag{1}$$

where x_{cor} is in μm, i_{cor} is the current density in μA/cm^2, t is time in days, and 0.032 is a factor to convert μm/day into μA/cm^2. This approach assumes that the corrosion penetration x_{cor} is much smaller than the diameter of the steel reinforcement bar, which is valid for the modelling carried out [31].

The calibration procedure for the lattice model was carried out in multiple steps. In the first step, the two elastic parameters E and a_1 were determined from a direct tensile test without taking creep into account using the reference elastic properties of the concrete (E^{ref} and ν^{ref}) for each of the four mixes in Table 1. The dimensions of the specimen for determining the elastic properties are 75 mm$\times$50 mm$\times$10 mm. In this test, the load is applied in the long direction of the specimen.

The next step is to determine the parameters for basic creep which are q_1, q_2, q_3 and q_4 on a single element tested in uniaxial tension, first using the formulas in Bažant and Baweja [8] to calculate the parameters then scaling them to obtain the desired Young's modules of lattice material E that is obtained from the previous step. In this single-element test, the load is applied at the age of 28 days for a loading duration of 0.01 days.

The next calibration step is carried out on a direct tensile test to obtain the inelastic parameters $f_{\text{t}}^{\text{ref}}$ and $G_{\text{f}}^{\text{ref}}$. In this test, the end regions are set as elastic to avoid cracks at the boundaries, so that only 50 mm of the middle region is able to fracture. The randomness of the material strength is considered for the lattice model by an autocorrelated random field with a Gaussian probability function of fully correlated strength and fracture energy [23]. The chosen autocorrelation length is $l_{\text{a}} = 2.67$ mm, and the coefficient of variation of the random field is $c_{\text{v}} = 0.2$. In this step of the calibration process, six analyses with different random fields and meshes for the four concrete mixes are carried out. The input parameters of these analyses for each concrete mix f_{t} and w_{f} are chosen to determine a mean tensile strength and fracture energy from the analyses that agree with the reference prop-

erties for the four mixes. The other parameters of the lattice model are set to the default values as presented in the manual of OOFEM [33].

5 RESULTS

The results of experiments and simulations are presented in the form of crack opening versus corrosion penetration curves and crack patterns. For the crack opening versus corrosion penetration curves, the mean, maximum and minimum value of the crack opening are shown for a given corrosion penetration. In Figure 8, crack opening versus corrosion penetration curves for the four mixes and a current density of 500 μA/cm^2 are shown.
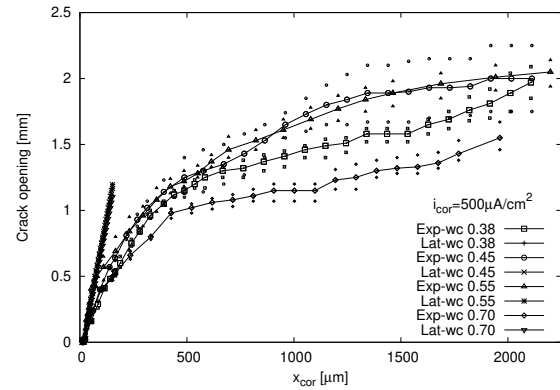
Figure 8: Crack opening versus corrosion penetration for $i_{\text{cor}} = 500\ \mu$A/cm^2.

For this current density, concrete with a very high water-cement ratio requires a higher corrosion penetration for the same crack opening than other water-cement ratios. For the other water-cement ratios, the effect of water-cement ratio on crack opening for a constant corrosion penetration is not clear. From the lattice model results it can be seen that the crack width for a given corrosion penetration is much smaller than in the experiments. The effect of water-cement ratio on crack opening for a constant corrosion penetration is very small too.
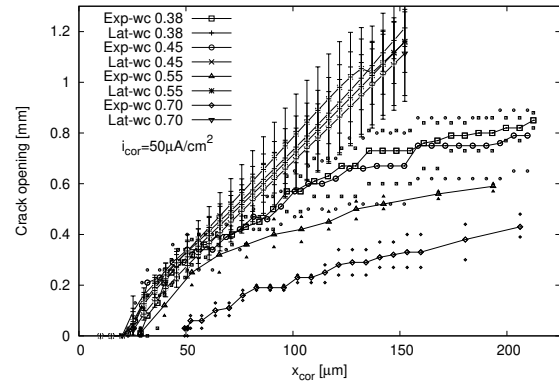
In Figure 9, crack opening versus corrosion penetration curves for four mixes and a current density of $i_{\text{cor}} = 100\ \mu$A/cm^2 are shown.
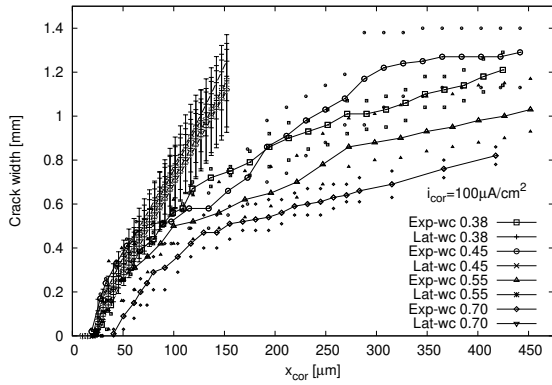
Figure 9: Crack opening versus corrosion penetration for $i_{\text{cor}} = 100 \ \mu\text{A/cm}^2$.

Figure 10: Crack opening versus corrosion penetration for $i_{\text{cor}} = 50 \ \mu\text{A/cm}^2$.

Again, for the high water-cement ratio of 0.7 more corrosion penetration is required for a given crack opening than for the other water-cement ratios. For the lattice modelling results, the effect of water-cement ratio is stronger than for $i_{\text{cor}} = 500 \ \mu\text{A/cm}^2$, but still much less than in the experiments. Again, the crack opening for a fixed corrosion penetration obtained with the model is much less than in the experiments.

Finally, in Figure 10, crack opening versus corrosion penetration curves for four mixes and current density of $i_{\text{cor}} = 50 \ \mu\text{A/cm}^2$ are shown. There is a strong influence of the water-cement ratio on the amount of the required corrosion penetration to obtain the same crack opening. For instance, it can be seen that for a 0.3 mm crack width the corrosion penetration for a concrete mix with a high water-cement ratio of 0.70 is three times higher than that for a small water-cement ratio of 0.45. For this current density, the modelling results still underestimate the crack openings obtained in the experiments. However, the difference between model and experiment is less pronounced than for the higher current densities.

Is should be noted that the corrosion process was initiated at a time at which the concrete was mature, as shown in Table 1. Therefore, creep is less pronounced than for concrete at 28 days.

The lattice model is based on a three-dimensional discretisation of the cylinder, which provides detailed information about force distributions and crack patterns at different stages of the analysis. That allows us to make a comparison between the crack patterns from the lattice model and experiment specimens as shown in Figure 11, which presents the crack patterns for wc0p45 with three current densities ($i_{\text{cor}} = 50$, 100 and 500 $\mu\text{A/cm}^2$). Since the geometry of the specimen is axis-symmetric and the applied corrosion is uniform with respect to the circumference of the bar, the crack orientation of the main crack which reaches the surface is random. To be able to compare well experiments and simulations, the experimental crack patterns were rotated so that the directions of the main cracks in experiments and simulations are aligned.

It should be noted that the crack width in the experimental specimens are different because the photos were taken at the same time and a higher current density provided a bigger crack at the same duration. For the lattice model the crack patterns are shown for the same corrosion penetration. The colour red (dark grey in black and white) corresponds to an equivalent crack width of $\bar{w}_c > 2 \ \mu\text{m}$.

7
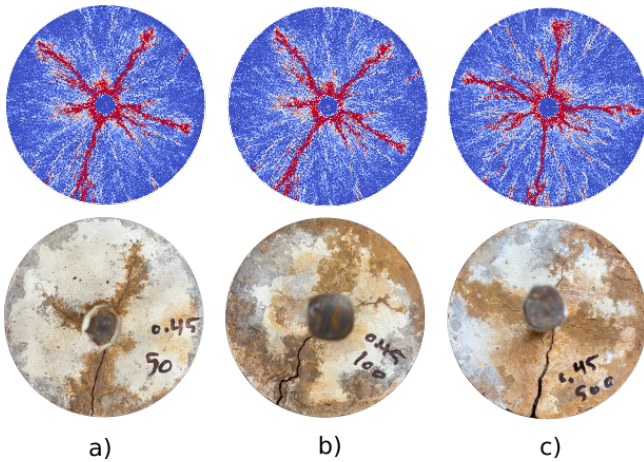
Figure 11: The crack patterns after the concrete cover cracked from the lattice model and experiment for the three current densities: a) $i_{\mathrm{cor}} = 50$ μA/cm^2, b) 100 μA/cm^2 and c) 500 μA/cm^2.

6 CONCLUSIONS

The main aim of the study was to investigate if fracture and linear creep modelled by a lattice approach can predict the effect of current density and water-cement ratio on corrosion-induced cracking observed in experiments carried out in this study. Comparing the results from the lattice modelling and the experiments, it can be concluded that the lattice modelling approach with fracture and linear creep alone underestimates the crack opening obtained in the experiments for the same corrosion penetration. This underestimation is particularly strong for high current densities. For low current densities, an increase in the water-cement ratio increases the crack opening at a constant corrosion penetration for the lattice modelling. However, this increase is still less than observed in the experiments. Therefore, our results indicate that fracture and creep alone is not sufficient to predict the crack-opening versus corrosion penetration curves obtained in experiments. The modelling framework is also not sufficient to model the effect of water-cement ratio on crack opening versus corrosion penetration accurately. Therefore, it is required to consider in addition other processes in the modelling framework such as migration of corrosion products and change of composition of corrosion products as a function of current density.

References

[1] Ahmad, Z. *Principles of corrosion engineering and corrosion control*. Elsevier, 2006.

[2] Aldellaa, I.; Havlásek, P.; Jirásek, M., and Grassl, P. Effect of creep on corrosion-induced cracking. *Engineering Fracture Mechanics*, page 108310, 2022.

[3] Almusallam, A. A.; Al Gahtani, A. S.; Aziz, A. R., and Rasheeduzzafar, . Effect of reinforcement corrosion on bond strength. *Construction and building materials*, 10(2):123–129, 1996.

[4] Alonso, C.; Andrade, C.; Rodriguez, J., and Diez, J. Factors controlling cracking of concrete affected by reinforcement corrosion. *Materials and Structures*, 31(7): 435–441, 1998.

[5] Andrade, C. and Alonso, C. On-site measurements of corrosion rate of reinforcements. *Construction and building materials*, 15(2-3):141–145, 2001.

[6] Andrade, C.; Alonso, C., and Molina, F. J. Cover cracking as a function of bar corrosion: Part I-Experimental test. *Materials and Structures*, 26(8):453–464, 1993.

[7] Athanasiadis, I.; Wheeler, S. J., and Grassl, P. Hydro-mechanical network modelling of particulate composites. *International Journal of Solids and Structures*, 130–131:49–60, 2018.

[8] Bažant, Z. P. and Baweja, S. Short form of creep and shrinkage prediction model B3 for structures of medium sensitivity. *Materials and Structures*, 29:587–593, 1996. Addendum to RILEM Recommendation TC 107-GCS.

[9] Bažant, Z. P. and Oh, B.-H. Crack band theory for fracture of concrete. *Materials and Structures*, 16:155–177, 1983.

[10] Bažant, Zdeněk P and Jirásek, Milan. *Creep and hygrothermal effects in concrete structures*, volume 38. Springer, 2018.

[11] Bolander, J. E. and Saito, S. Fracture analysis using spring networks with random geometry. *Engineering Fracture Mechanics*, 61:569–591, 1998.

[12] Broomfield, J. P. *Corrosion of steel in concrete: understanding, investigation and repair*. Taylor & Francis, 1997.

[13] Caballero, A.; Lopez, C., and Carol, I. 3d meso-structural analysis of concrete specimens under uniaxial tension. *Computer Methods in Applied Mechanics and Engineering*, 195(52):7182–7195, 2006.

[14] Castel, Arnaud; Vidal, Thierry; François, Raoul, and Arliguie, Ginette. Influence of steel–concrete interface quality on reinforcement corrosion induced by chlorides. *Magazine of Concrete Research*, 55 (2):151–159, 2003.

[15] CEB-FIP. *CEB-FIP Model Code 2010, Design Code*, 2012.

[16] Cundall, P. A. and Strack, O. D. L. A discrete numerical model for granular assemblies. *Géotechnique*, 29:47–65, 1979.

[17] Cusatis, G.; Bažant, Z. P., and Cedolin, L. Confinement-shear lattice csl mode for fracture propagation in concrete. *Computer Methods in Applied Mechanics and Engrg.*, 195:7154–7171, 2006.

[18] El Maaddawy, T. and Soudki, K. A. Effectiveness of impressed current technique to simulate corrosion of steel reinforcement in concrete. *Journal of materials in civil engineering*, 15(1):41–47, 2003.

[19] Fahy, C.; Wheeler, S.; Gallipoli, D., and Grassl, P. Corrosion induced cracking modelled by a coupled transport-structural approach. *Cement and Concrete Research*, 94:24–35, 2017.

[20] François, Raoul and Arliguie, Ginette. Influence of service cracking on reinforcement steel corrosion. *Journal of Materials in Civil Engineering*, 10(1):14–20, 1998.

[21] Grassl, P. and Davies, T. Lattice modelling of corrosion induced cracking and bond in reinforced concrete. *Cement and Concrete Composites*, 33:918–924, 2011.

[22] Grassl, P. and Jirásek, M. Damage-plastic model for concrete failure. *International Journal of Solids and Structures*, 43:7166–7196, 2006.

[23] Grassl, P. and Jirásek, M. Meso-scale approach to modelling the fracture process zone of concrete subjected to uniaxial tension. *International Journal of Solids and Structures*, 47:957–968, 2010.

[24] Grassl, Peter and Davies, Trevor. On a three-dimensional lattice approach for modelling corrosion induced cracking and its influence on bond between reinforcement and concrete. *arXiv preprint arXiv:1001.1442*, 2010.

[25] Jirásek, M and Havlásek, P. Microprestress–solidification theory of concrete creep: Reformulation and improvement. *Cement and Concrete Research*, 60:51–62, 2014.

[26] Jirásek, M. and Havlásek, P. Accurate approximations of concrete creep compliance functions based on continuous retardation spectra. *Computers and Structures*, 135:155–168, 2014.

[27] Kawai, T. New discrete models and their application to seismic response analysis of structures. *Nuclear Engineering and Design*, 48:207–229, 1978.

[28] Korec, E.; Jirásek, M.; Wong, H., and neda, E. Martínez-Pa˙ A phase-field chemo-mechanical model for corrosion-induced cracking in reinforced concrete.

Construction and Building Materials, 393:131964, 2023.

[29] Kuntal, Vikas Singh; Jiradilok, Punyawut; Bolander, John E, and Nagai, Kohei. Estimating corrosion levels along confined steel bars in concrete using surface crack measurements and mesoscale simulations guided by model predictive control. *Cement and Concrete Composites*, 124:104233, 2021.

[30] Mangat, P. S. and Elgarf, M. S. Flexural strength of concrete beams with corroding reinforcement. *Structural Journal*, 96(1): 149–158, 1999.

[31] Molina, F.; Alonso, C., and Andrade, C. Cover cracking as a function of rebar corrosion: Part II-numerical model. *Materials and Structures*, 26(9):532–548, 1993.

[32] Mullard, A. and Stewart, M. G. Corrosion-induced cover cracking: new test data and predictive models. *ACI Structural Journal*, 108(1):71, 2011.

[33] Patzák, B. OOFEM – An object-oriented simulation tool for advanced modeling of materials and structure. *Acta Polytechnica*, 52:59–66, 2012.

[34] Schlangen, E. and van Mier, J. G. M. Simple lattice model for numerical simulation of fracture of concrete materials and structures. *Materials and Structures*, 25:534–542, 1992.

[35] Schlangen, E and Van Mier, JGM. Simple lattice model for numerical simulation of fracture of concrete materials and structures. *Materials and Structures*, 25(9): 534–542, 1992.

[36] Standard, ASTM. G1-03. Standard Practice for preparing, cleaning, and evaluating corrosion test specimens, Annual Book of ASTM Standards, 3:17–25, 2003.

[37] Tuutti, K. Corrosion of steel in concrete. Doctoral thesis, Swedish Cement and Concrete Research Institute, 1982.

[38] Vu, Kim; Stewart, Mark G, and Mullard, John. Corrosion-induced cracking: experimental data and predictive models. *ACI structural journal*, 102(5):719, 2005.

[39] Yip, M.; Mohle, J., and Bolander, J. E. Automated Modeling of Three-Dimensional Structural Components Using Irregular Lattices. *Computer-Aided Civil and Infrastructure Engineering*, 20 (6):393–407, 2005.

[40] Zahid, Hafiza Fatima; Jiradilok, Punyawut; Kuntal, Vikas Singh, and Nagai, Kohei. Investigation of the effects of multiple and multi-directional reinforcement on corrosion-induced concrete cracking pattern. *Construction and Building Materials*, 283:122594, 2021.

[41] Zhang, R.; Castel, A., and François, R. Serviceability limit state criteria based on steel–concrete bond loss for corroded reinforced concrete in chloride environment. *Materials and structures*, 42(10): 1407, 2009.

[42] Zhang, R.; Castel, A., and François, R. The corrosion pattern of reinforcement and its influence on serviceability of reinforced concrete members in chloride environment. *Cement and Concrete Research*, 39(11):1077–1086, 2009.

[43] Zhang, Ruijin; Castel, Arnaud, and François, Raoul. Concrete cover cracking with reinforcement corrosion of rc beam during chloride-induced corrosion process. *Cement and Concrete Research*, 40(3):415–425, 2010.

[44] Zhang, W.; Chen, J., and Luo, X. Effects of impressed current density on corrosion induced cracking of concrete cover. *Construction and Building Materials*, 204: 213–223, 2019.

[45] Zubelewicz, A. and Bažant, Z. P. Interface modeling of fracture in aggregate composites. *Journal of Engineering Mechanics, ASCE*, 113:1619–1630, 1987.